Intrinsic Dirac half-metal and quantum anomalous Hall phase in a hexagonal metal-oxide lattice

Shou-juan Zhang,[1] Chang-wen Zhang,[1,*] Shu-feng Zhang,[1] Wei-xiao Ji,[1] Ping Li,[1] Pei-ji Wang,[1] Sheng-shi Li,[2] and Shi-shen Yan[2]

[1]*School of Physics and Technology, University of Jinan, Jinan, Shandong 250022, People's Republic of China*

[2]*School of Physics, State Key Laboratory of Crystal Materials, Shandong University, Jinan, Shandong 250100, People's Republic of China*

(Received 5 August 2017; revised manuscript received 3 November 2017; published 27 November 2017)

The quantum anomalous Hall (QAH) effect has attracted extensive attention due to time-reversal symmetry broken by a staggered magnetic flux emerging from ferromagnetic ordering and spin-orbit coupling. However, the experimental observations of the QAH effect are still challenging due to its small nontrivial bulk gap. Here, based on density functional theory and Berry curvature calculations, we propose the realization of intrinsic QAH effect in two-dimensional hexagonal metal-oxide lattice, Nb_2O_3, which is characterized by the nonzero Chern number ($C = 1$) and chiral edge states. Spin-polarized calculations indicate that it exhibits a Dirac half-metal feature with temperature as large as $T_C = 392$ K using spin-wave theory. When the spin-orbit coupling is switched on, Nb_2O_3 becomes a QAH insulator. Notably, the nontrivial topology is robust against biaxial strain with its band gap reaching up to $E_g = 75$ meV, which is far beyond room temperature. A tight-binding model is further constructed to understand the origin of nontrivially electronic properties. Our findings on the Dirac half-metal and room-temperature QAH effect in the Nb_2O_3 lattice can serve as an ideal platform for developing future topotronics devices.

DOI: 10.1103/PhysRevB.96.205433

I. INTRODUCTION

Topological phase and topological property have sparked extensive research interests in condensed-matter physics and materials science and won the Nobel Prize in physics in 2016. The quantum anomalous Hall (QAH) insulator [1–4] is a nontrivial phase where the ferromagnetic (FM) ordering and spin-orbit coupling (SOC) conspire to generate energy gap E_g in the bulk, and gapless chiral edge states at its edges. Its topologically nontrivial properties are characterized by a nonzero Chern number (C) counting the number edge states whose energy-momentum dispersion threads the gap of finite width nanoribbons, while their wave functions have finite spatial extent around the ribbon edges. Unlike the two-dimensional (2D) quantum spin Hall (QSH) insulator [5–9], where helical edge states appear in pairs with different chirality and spin polarization, the edge states of the QAH insulator allow only one spin species to flow unidirectionally. Thus, the edge state transport in nanoribbons made of QAH insulator is robust against defects, disorder, and surface contamination over hundreds of micrometers, which makes them superior to edge states of the QSH insulator where electrons can be backscattered by disorder with time-reversal symmetry (TRS) breaking [10]. These ground breaking discoveries introduce interesting physics principles and establish a solid foundation for understanding a different type of topological phase transition in 2D materials. Experimentally, the QAH effect in thin-film $(Bi, Sb)_2Te_3$ doped with Cr or V atoms has been reported at very low temperature [10,11], thus igniting intense searches for systems whose energy gap E_g and Curie temperature (T_C) are both far beyond room temperature [12]. Finding such 2D materials would open avenues for nanoelectronic devices with ultralow dissipation where edge states act as "chiral interconnects" whose resistance is independent of the length of the nanoribbons [13,14].

The seminal work on the Haldane model [15], where the quantized Hall conductance without Landau levels is introduced on a honeycomb lattice in the absence of an external magnetic field, has inspired extensive attention for realistic materials exhibiting QSH or QAH states where the honeycomb lattice is suggested as a first ingredient [16,17]. Subsequently, some 2D crystals are proposed, including graphene decorated with heavy 5d transition metals [18] or heterostructures like graphene/FM-insulator [19]. Honeycomb lattice composed of silicene, germanene, and stanene, which already possess strong intrinsic SOC, could also be converted into QAH phase by introducing exchange interaction via magnetic adatoms [20] or surface functionalization [21]. These 2D stoichiometric magnetic honeycomb lattices, however, exist rarely in nature and are difficult experimentally to manipulate due to their structural complexity while keeping the topology of these systems unaffected. The experimental realization of these exciting QAH phases is still in its infancy.

In the present work, we propose that a 2D hexagonal metal-oxygen lattice, Nb_2O_3, can host an intrinsic QAH insulating state, which is characterized by nonzero Chern number ($C = 1$) and chiral edge states. Spin-polarized calculations indicate that it exhibits a Dirac half-metal feature with Curie temperature of $T_C = 392$ K which, with turning on SOC, becomes a QAH insulator. Notably, the nontrivial topology is robust against biaxial strain, with its band gap reaching up to $E_g = 75$ meV, which is much larger than the recently predicted $E_g = 20$ meV in the kagome lattice $Cs_2Mn_3F_{12}$ [22] and $E_g = 2.3$ meV in Mn-dicyanoanthracene (Mn-DCA) lattice [23]. In comparison to Cr- or V-doped $(Bi, Sb)_2Te_3$ films [10,11], such a lattice without any magnetic doping is easier to synthesize and has a much higher homogeneity. These findings on the Nb_2O_3 lattice open a direction for the exploration of the topological states of matter.

*ss_zhangchw@ujn.edu.cn

The rest of the paper is organized as follows. In Sec. II we describe the theoretical methods used for our calculations of Nb_2O_3 lattice. In Sec. III the stability, electronic, and topological properties are discussed. Finally, we draw our conclusions on Nb_2O_3 lattice in Sec. VI.

II. COMPUTATIONAL DETAILS

Spin-polarized calculations are performed by using density-functional theory (DFT), as implemented in Vienna *ab initio* simulation package (VASP) [24]. The projector- augmented-wave (PAW) potential [25,26], Perdew-Burke -Ernzerhof (PBE) exchange-correlation functional [27], and the plane-wave basis with a kinetic-energy cutoff of 500 eV are employed. To describe the strongly correlated 4*d* electrons of the Nb atom, the GGA + U method is employed. Here, the difference between the on-site Coulomb (U) and exchange parameter (J) is set to 3.0 eV (U-J) in the calculations, which is consistent with the one of $Nb(TCNE)_2$. [28] The Brillouin zone is sampled by using an $11 \times 11 \times 1$ Γ-centered Monkhorst - Pack grid, and the SOC is included by a second variational procedure on a fully self-consistent basis. During structural optimization, all atomic positions and lattice parameters are fully relaxed, and the maximum force allowed on each atom is less than 0.02 eV/Å. Furthermore, the screened exchange hybrid density functional by Heyd-Scuseria-Ernzerhof (HSE06) [29] is adopted to check the electronic structure. The phonon calculations are carried out by using DFT perturbation theory as implemented in the PHONOPY code [30] combined with VASP.

III. RESULTS AND DISCUSSION

A. Structure and stability of Nb_2O_3 lattice

Figure 1(a) shows the geometric structure of the Nb_2O_3 lattice, where Nb atoms form a honeycomb lattice with a threefold rotational symmetry by sharing one oxygen (O) bridge with each neighbor, accompanied by its Brillouin zone (BZ) in Fig. 1(c). In comparison to the organic kagome lattice [31–33], here the oxygen atoms substitute for triangular

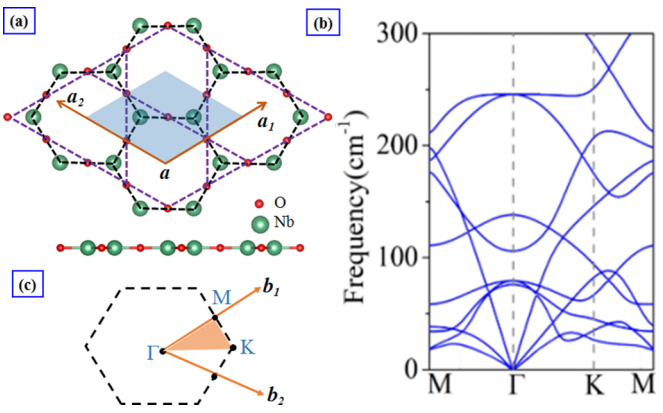

FIG. 1. (a) Top and side view of Nb_2O_3 with lattice vectors a_1 and a_2 in the xy plane. Rhombus shows the unit cell. (b) The calculated phonon spectrum. (c) The first Brillouin zone of the Nb_2O_3 lattice with reciprocal-lattice vectors b_1 and b_2.

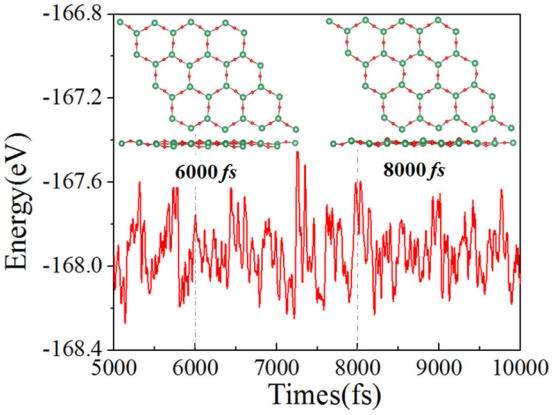

FIG. 2. Variation of the energy from 5000 to 10000 fs during MD simulations at a temperature of 600 K for Nb_2O_3 lattice. The inset illustrates a snapshot of the MD simulation of the structure at temperatures of 6000 and 8000 fs, respectively.

organic molecules. Structural optimizations indicate that the 2D Nb_2O_3 lattice is flat with the Nb and O atoms moving alternately in the same plane, which is depicted by the top and side view in Fig. 1(a). The lattice constant is $a_1 = a_2 = 6.60$ Å with the Nb-Nb distance of 3.86 Å. The structural stability is examined by calculating the formation energy expressed as $\Delta E_f = E(Nb_2O_3) – 2E(Nb) – 3/2\mu$ (O_2), where E (Nb_2O_3) and E (Nb) are the total energies of the Nb_2O_3 and Nb crystals, respectively, while $\mu(O_2)$ is the chemical potential oxygen gas. The obtained negative value, −5.34 eV, indicate that the Nb_2O_3 lattice is a strongly bonded network and thus favors its experimental synthesis. To examine whether the Nb_2O_3 becomes buckled, we construct the buckled Nb_2O_3 lattice, similar to the case of MoS_2 and CrI_3 configurations. The calculated energy differences between planar and different buckled configurations are shown in Fig. S1 of the Supplemental Material [34]. One can see that, with the increase of buckle height from 0 to 1.8 Å, the energies of Nb_2O_3 increase monotonically. This indicates that the planar configuration has the lowest energy, and thus is the most stable structure.

To test the kinetic stability of the Nb_2O_3 lattice, we further perform the phonon spectrum calculations. As shown in Fig. 1(b), no appreciable imaginary phonon modes are observed, indicating that the Nb_2O_3 lattice is kinetically stable. Additionally, the thermal stability of Nb_2O_3 lattice is assessed by performing *ab initio* molecular dynamics (MD) simulations. We use a 3×3 supercell to carry out the individual MD simulations at temperatures of 300, 400, 500, and 600 K, respectively. Snapshots of Nb_2O_3 lattice at 6000 and 8000 fs are plotted for these structures, as illustrated in Fig. 2 and in Fig. S2 of the Supplemental Material [34]. Note that the structure of Nb_2O_3 lattice does not collapse throughout a 10-ps MD simulation up to 600 K, indicating that the melting point of Nb_2O_3 lattice is probably 600 K. The above results reveal that the Nb_2O_3 lattice has very good thermal stability and can maintain its structural integrity in a high-temperature environment. In previous works [35], the Y_2O_3 lattice has been reported to form a complete monolayer on platinum-supported graphene. The monolayer interacts weakly with graphene, but is stable to high temperature. Scanning tunneling microscopy

reveals that the Y_2O_3 exhibits a two-dimensional hexagonal lattice rotated by 30° relative to the hexagonal graphene lattice. More recently, by using the PSO search and VASP simulations, Song *et al.* [36] predict that the planar Al_2O_3 monolayer with a hexagonal lattice is stable and can be realized experimentally. Obviously, all these results provide solid evidence to support our predictions.

B. FM ordering and Curie temperature

After having established that the Nb_2O_3 lattice is structurally stable, we then investigate its magnetic properties. Note that the ground state of Nb_2O_3 lattice is strongly spin polarized with a local magnetic moment of 2.0 μ_B per Nb atom, corresponding to spin configuration $d^2\uparrow^0\downarrow$. This is because each Nb atom is threefold coordinated to an oxygen atom, thus the formal valence of Nb atom is Nb^{3+}, which is confirmed by Bader charge analysis. Hund's rule would then give spin $S = 1$ on each Nb atom. To determine the preferred ground state, we calculate the FM and antiferromagnetic (AFM) spin orientations, and find that the total energies of the FM state are 0.74 eV/f.u. lower than the AFM state, indicating the FM state is more stable. If the 2D spin system is isotropic, Mermin and Wagner [37] demonstrate that the strong thermal fluctuations of gapless long-wavelength modes will destroy the 2D FM ordering at finite temperature. So the model Hamiltonian for the spins of Nb atoms in the honeycomb lattice should be expressed as [38]

$$H = -\left(\sum_i D\left(S_i^z\right)^2 + \frac{J}{2}\sum_{i,i'}\vec{S}_i\cdot\vec{S}_{i'} + \frac{\lambda}{2}\sum_{i,i'}S_i^Z S_{i'}^Z\right), \quad (1)$$

where the sum i runs over the entire lattice of Nb atoms, and the sum i' runs over the 3 Nb atoms (the first neighbors of atom i). The first term in the Hamiltonian describes the easy axis single-ion anisotropy defined z as the off-plane direction. The second term is the isotropic exchange and the final term is the anisotropic symmetric exchange. The sign convention is such that $J > 0$ favors FM interactions. In this case, we consider the energies of four possible ground states, i.e., FM off-plane (FM, z), AFM off-plane (AFM, z), FM in-plane (FM, x), and AFM in-plane (AFM, x). So, the spin model allows writing the energetics of the different configurations normalized per unit cell as

$$\begin{aligned}
\varepsilon_{\mathrm{FM,z}} &= -3S^2(J+\lambda) - 2S^2D,\\
\varepsilon_{\mathrm{AFM,z}} &= +3S^2(J+\lambda) - 2S^2D,\\
\varepsilon_{\mathrm{FM,x}} &= -3S^2J,\\
\varepsilon_{\mathrm{AFM,x}} &= +3S^2J.
\end{aligned} \quad (2)$$

In order to determine J and λ, by comparing the total energies of FM and AFM states with the spins orientating along the in-plane and out-of-plane directions, we obtain that $J = 123$ meV, $\lambda = 0.2$ meV, and $D = 0.002$ meV, respectively. Based on spin-wave theory, we can provide a rough estimate of the Curie temperature, expressed as

$$M = S - \frac{1}{2(2\pi)^2}\int_{\mathrm{BZ}}\frac{d^2\vec{k}}{e^{\beta ME(k)/S} - 1}, \quad (3)$$

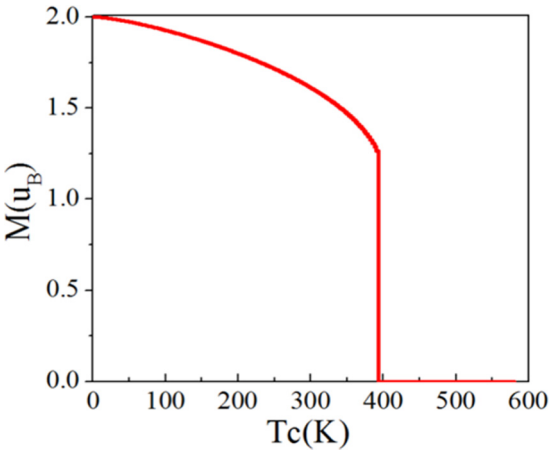

FIG. 3. Self-consistent solution of the magnetization derived with Eq. (3), showing a depleted magnetization with increasing temperature.

where the integral extends over the first BZ, and the units of both M and S are $\hbar$. As Eq. (3) has no solution for $M = 0$, we can obtain a self-consistent solution of the Curie temperature in Fig. 3, $T_C = 392$ K, which is far beyond room temperature.

Generally, the AFM state is energetically more stable than the FM state according to conventional superexchange interaction at 180°. [37] However, it doe snot hold true for all cases, including 2D materials. In the Nb_2O_3 lattice, the strong ferromagnetism originates mainly from half-filled d_{xz} and d_{yz} bands, as shown in Fig. 5. Due to the strong orbital hybridization of spin-up d_{xz} and d_{yz} orbitals of Nb atoms through the interbridged oxygen atom, the twofold degenerate d_{xz} and d_{yz} states would split into the low-lying bonding and high-lying antibonding states, as illustrated in Fig. 4. Considering the Nb^{3+} spin configuration, the remaining two d electrons with the same FM spin alignment would occupy the low-lying bonding ($|xz^+\rangle$and$|yz^+\rangle$) states, thus resulting in an energy lowering, since E (FM) is proportional to t, where t is the hopping between neighboring Nb atoms. However, if the spins of two Nb^{3+} atoms are antiparallel to each other, the energy E(AFM) would decrease if E(AFM) is proportional to t^2/U due to the superexchange model. Since Hubbard U is generally larger than t, the system favors FM ordering. Obviously, the origin of ferromagnetism is due to direct

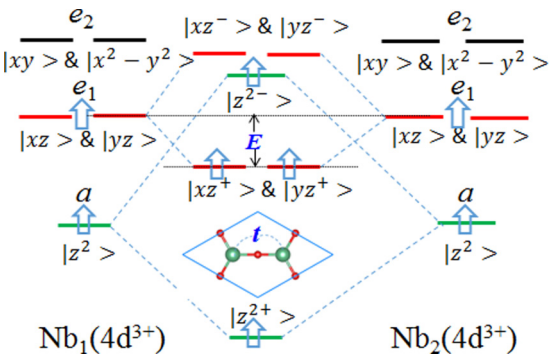

FIG. 4. The plot of exchange mechanism for the FM ordering. The inset gives the hopping parameter t in Nb_2O_3 lattice.

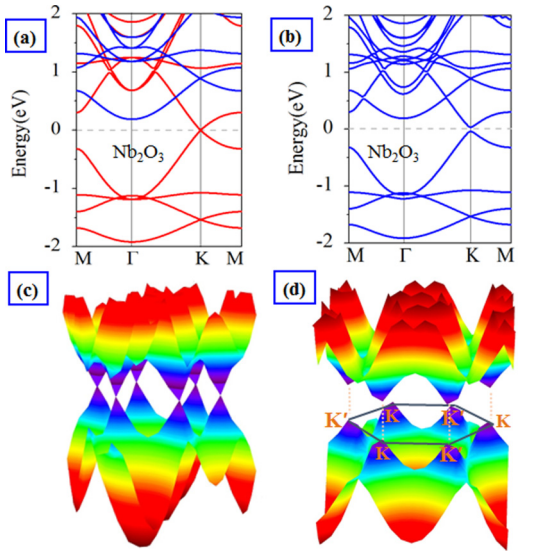

FIG. 5. (a), (b) Band structures of the Nb_2O_3 lattice without and with SOC, respectively. Red and blue solid lines denote spin-up and spin-down bands. (c), (d) 3D band profile around the Fermi level corresponding to (a) and (b), respectively.

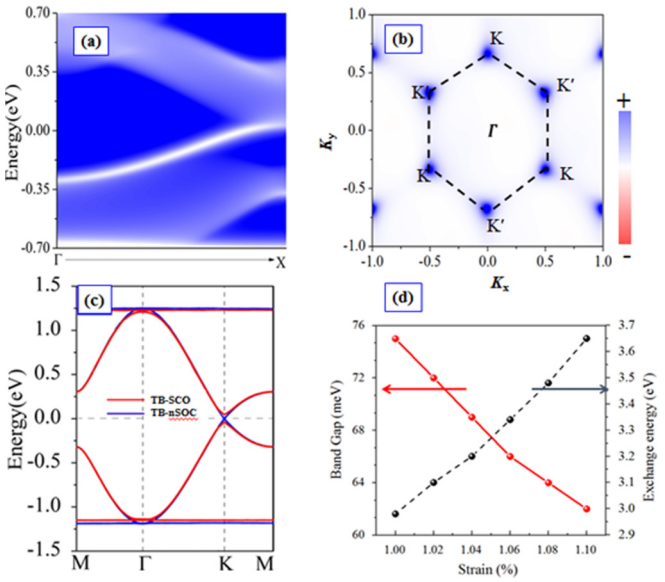

FIG. 6. (a) The chiral edge states of the Nb_2O_3 lattice. (b) Berry curvature with SOC in the momentum space. The red, white, and blue colors give distribution of Berry curvature from positive to negative value, and the black dashed lines show first BZ. (c) Band structures of Nb_2O_3 calculated using the TB model with and without SOC. (d) The global gap E_g and the total-energy difference as a function of the biaxial strain.

exchange between Nb orbitals, and the ferromagnetism can be understood as a Stoner instability of an itinerant electron gas. Additionally, the results are confirmed by GGA + U calculations in Fig. S3 of the Supplemental Material [34], where the energy difference between the FM and AFM states increases monotonically as a function of U. The possible reason can be attributed to that the energy in the AFM state decreases significantly with U, while that in the FM case does not depend on U. Therefore, we can infer that the excellent magnetic and electronic properties of Nb_2O_3 show a favorable robustness against the correction effect, as illustrated in Fig. S4 of the Supplemental Material [34].

C. Electronic properties of Nb_2O_3 lattice

We now proceed to study the electronic properties of Nb_2O_3 lattice. Figure 5(a) shows the calculated band structures without SOC, where the red and blue lines display the spin-up and spin-down channels, respectively. Because of internal magnetization, the spin-up and spin-down bands are completely split away from each other, and only the spin-up band is left around the Fermi level. From the 3D band profile near the K point, we also observe a clear linear Dirac cone, with the Fermi level located exactly at the Dirac point. Notably, this is a typical kagome band around the Fermi level, consisting of two completely flat bands above two Dirac bands remaining at the K point, as illustrated in Fig. 5(c). Note that the spin-down channel possesses a semiconducting behavior with a gap of 0.78 eV, while the spin-up one has partially filled metallic bands, showing a half-metallic character with 100% spin-polarized currents. We also observe that the bands near the Fermi level are mainly composed of Nb-d orbital where the Dirac cone is mainly contributed by $d_{xz,yz}$ states, while the contributions from s and p orbitals are negligible. On this occasion, the Fermi velocity (v_F) of Dirac fermions at the Fermi level is evaluated as 4.6×10^5 m/s, in consistent with one of graphene (8×10^5 m/s) [39]. The existence of spin-polarized Dirac fermions in one spin channel and large band gap in another channel constitute a great potential for applications in spintronics.

D. QAH effect in Nb_2O_3 lattice

Dirac materials, such as in IV-based 2D honeycomb lattice [40], are generally characterized by Dirac states composed of a p orbital with weaker SOC. Thus, SOC opens just a tiny gap, forming Z_2 topological insulators (TIs) with TRS protected edge states. The Dirac states of 2D Nb_2O_3 lattice, however, are mainly derived from the Nb d orbital. The strong strength of SOC induced by the d orbital, accompanied with broken TRS, may lead to a QAH phase. Indeed, our DFT calculations demonstrate that the switch on SOC results in a gap of E_g = 75 meV at the K point, as shown in Figs. 4(b) and 4(d), which is much larger than the recently predicted E_g = 20 meV in the kagome lattice $Cs_2Mn_3F_{12}$ [22] and E_g = 2.3 meV in the Mn-DCA lattice [23]. To show the nontrivial topology of this lattice, we construct the Green's functions [41] for the semi-infinite boundary based on the maximally localized Wannier function method [42,43]. Figure 6(a) displays the calculated local density of state (LDOS) of the edge states. Obviously, the nontrivial edge states connecting the valence and conduction bands cross the insulating gap of the spin-up Dirac cone. The existence of chiral edge states inside such a large band gap is a manifestation of the band topology of bulk Bloch states of valence bands.

E. Tight-binding model of QAH effect

In order to get more insights into the origin of the QAH effect, we now focus on the orbital-projected electronic band structures of 2D Nb_2O_3 lattice. As seen from Fig. 5, the Dirac bands are mainly composed of d_{xz} and d_{yz} orbitals, and overlap with little contributions from O $2p$ orbital in proximity of the Fermi level. Despite the inner magnetism, the spin-up and spin-down bands are no longer separable when considering SOC, but the z component of the spins (σ^z) is a conserved quantum number since the magnetic order of Nb_2O_3 is perpendicular to the xy plane. Thus the Hamiltonian conserves the z component of the spins, and we can divide the one-particle Hilbert space H into $H\uparrow \oplus H\downarrow$ by the eigenvalue of σ^z. Hence, we present the space $H\uparrow$ by constructing TB Hamiltonian (H_0) in combination with an SOC term ($H_{\rm SOC}$) including d_{xz} and d_{yz} orbitals of Nb atoms, since there are only spin-up bands across to the Fermi energy. In the basis of $(d_{A,xz}, d_{A,yz}, d_{B,xz}, d_{B,yz},)^T$, the hopping term without SOC can be written as

$$H_0 = t\sum_{i,j}\left(d^{\dagger}_{j,\vec{R}_i} d_{j,\vec{R}_i+,\vec{e}_j} + \text{H.c.}\right), \tag{5}$$

where $\overrightarrow{R}_i = m_i\vec{a} + n_i\vec{b}$ denotes the lattice points of A and B sites; $\vec{\delta}_j$ is the displacement from a unit cell to its neighboring unit cells; $\Gamma = xz, yz$ distinguishes different d orbitals, and $d_j = (d_{xz}\vec{e}_x + d_{yz}\vec{e}_y)\cdot\vec{e}_j$.

To include the SOC effect in TB calculations, we consider the on-site term $H_{\rm SOC}$ expressed as

$$H_{\rm SOC} = i\lambda\sum_i\left[\left(d^{\dagger}_{xz,\vec{R}_i} d_{yz,\vec{R}_i} - d^{\dagger}_{yz,\vec{R}_i} d_{xz,\vec{R}_i}\right) + \left(d^{\dagger}_{xz,\vec{R}_i^{(B)}} d_{yz,\vec{R}_i^{(B)}} - d^{\dagger}_{yz,\vec{R}_i^{(B)}} d_{xz,\vec{R}_i^{(B)}}\right)\right] \tag{6}$$

in which λ describes the strength of SOC. Finally the effective Hamiltonian can be expressed as

$$H(\vec{k}) = \begin{pmatrix} -\lambda + \frac{\epsilon_{Axz}+\epsilon_{Ayz}}{2} & \frac{\epsilon_{Axz}-\epsilon_{Ayz}}{2} & \frac{t}{2}g(\vec{k}) & \frac{t}{2}l(\vec{k}) \\ \frac{\epsilon_{Axz}-\epsilon_{Ayz}}{2} & \lambda + \frac{\epsilon_{Axz}+\epsilon_{Ayz}}{2} & \frac{t}{2}m(\vec{k}) & \frac{t}{2}g(\vec{k}) \\ \frac{t}{2}g^*(\vec{k}) & \frac{t}{2}m^*(\vec{k}) & -\lambda + \frac{\epsilon_{Bxz}+\epsilon_{Byz}}{2} & \frac{\epsilon_{Bxz}-\epsilon_{Byz}}{2} \\ \frac{t}{2}l^*(\vec{k}) & \frac{t}{2}g^*(\vec{k}) & \frac{\epsilon_{Bxz}-\epsilon_{Byz}}{2} & \lambda + \frac{\epsilon_{Bxz}+\epsilon_{Byz}}{2} \end{pmatrix}, \tag{7}$$

where

$$\begin{aligned} g(\vec{k}) &= e^{i\vec{k}\cdot\vec{e}_1} + e^{i\vec{k}\cdot\vec{e}_2} + e^{i\vec{k}\cdot\vec{e}_3}, \\ l(\vec{k}) &= \frac{1-i\sqrt{3}}{2}e^{i\vec{k}\cdot\vec{e}_1} + \frac{1+i\sqrt{3}}{2}e^{i\vec{k}\cdot\vec{e}_2} - e^{i\vec{k}\cdot\vec{e}_3}, \\ m(\vec{k}) &= \frac{1+i\sqrt{3}}{2}e^{i\vec{k}\cdot\vec{e}_1} + \frac{1-i\sqrt{3}}{2}e^{i\vec{k}\cdot\vec{e}_2} - e^{i\vec{k}\cdot\vec{e}_3}, \\ \vec{k}\cdot\vec{e}_1 &= \frac{\sqrt{3}}{2}k_x + \frac{1}{2}k_y, \quad \vec{k}\cdot\vec{e}_2 = \frac{-\sqrt{3}}{2}k_x + \frac{1}{2}k_y, \\ \vec{k}\cdot\vec{e}_3 &= -k_y. \end{aligned} \tag{8}$$

Figure 6(c) displays the calculated band structures with and without SOC, respectively. Note that the linear Dirac bands along the high-symmetry directions cross at the K point without SOC, and the flat bands and dispersive bands touch at the center of the first BZ, while the degeneracy of the Dirac cones between the middle two dispersive bands is also lifted. When the SOC is switched on, a sizeable gap of 75 meV opens, which is consistent with the DFT results. These demonstrate that the intrinsic SOC in Nb_2O_3 lattice is responsible for band gap opening at the Dirac bands, which is of importance to realize the QAH effect.

To further determine the nontrivial topology of Nb_2O_3 lattice, we calculate the Berry curvature $\Omega(k)$ from the Kubo formula [44,45] expressed by

$$\Omega(k) = \sum_n f_n\Omega_n(k), \tag{9}$$

$$\Omega_n(k) = -2\text{Im}\sum_{m\neq n}\frac{\langle\Psi_{nk}|\upsilon_x|\Psi_{mk}\rangle\langle\Psi_{mk}|\upsilon_y|\Psi_{nk}\rangle\hbar^2}{(E_m - E_n)^2}, \tag{10}$$

where the summation is over all of the occupied states, $E_{\rm n}$ is the eigenvalue of the Bloch function $|\Psi_{nk}\rangle$, $f_{\rm n}$ is the Fermi-Dirac distribution function, and $\upsilon_{\rm x}$ and $\upsilon_{\rm y}$ are the velocity operators. By using the TB Hamiltonian parametrization of Wannier functions with the WANNIER90 package [46,47], we obtain the Berry curvature for the whole valence bands along the high-symmetry directions and the corresponding 2D distribution in momentum space. As shown in Fig. 6(b), the nonzero curvatures are localized around K and K_0 points with the same sign. By integrating the Berry curvatures over the first BZ, we find that the Chern number (C), expressed as

$$C = \frac{1}{2\pi}\sum_n\int_{\rm BZ} d^2k\Omega_n, \tag{11}$$

is equal to 1 with each Dirac cone (K and K') contributing 0.5. In this case, the anomalous Hall conductivity σ_{xy}, $\sigma_{xy} = \frac{e^2}{h}C$ shows a quantized charge Hall plateau of at a value of $\frac{e^2}{h}$ located in the insulating gap of the spin-up Dirac cone. Such a nonvanishing Chern number and quantized Hall conductivity characterizes the QAH phase in the Nb_2O_3 lattice.

After confirming the nontrivial topology of the Nb_2O_3 lattice, we further check the robustness of the topological properties against external strain, in that the strain generally changes the SOC-induced bulk gap and spin exchange constant J_0. Figure 6(d) shows the evolution of direct gap E_g and FM exchange energy as a function of strain ε, which is defined as $(a - a_0)/a_0$, where $a(a_0)$ is the strained (equilibrium) lattice constants. Note that the nontrivial topological states remain within the strain range of 10%. This suggests that the Nb_2O_3 lattice maintains a topologically nontrivial state, which is stable against external strains. The gap E_g decreases with the

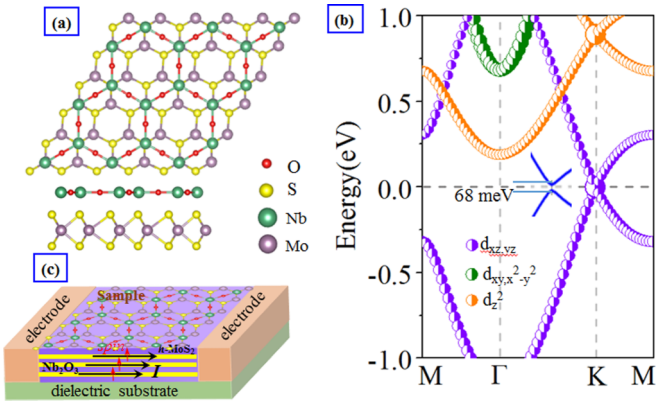

FIG. 7. (a) Top and side view of the epitaxial growth of the Nb_2O_3 lattice on MoS_2 substrate. (b) The corresponding energy band structure with SOC. The purple, green, and yellow dots denoted the $d_{xz,yz}$,$d_{xy,x2-y2}$ and d_{z2} orbital of Nb atoms, respectively. (c) Schematic device model for proposed Nb_2O_3/MoS_2 heterostructure for quantum state measurement. Vertical arrows show the spin orientation of electrons in the edge states and horizontal arrows show their transport directions.

strain, becoming 56.8 meV at the strain of 10%. However, the biaxial strain enhances the spin-exchange strength, and thus can effectively promote the Curie temperature to a high value.

On the other hand, we check the calculated results for the Nb_2O_3 lattice with HSE06 functional here. We find that a larger gap of 0.11 eV is obtained with zero strain, which is far beyond room temperature. It is noticeable that, though the bulk gap is enhanced for the HSE06 method, the d_{xz} and d_{yz} band character is not altered near the Fermi level, indicating that the nontrivial topology is robust to computational method.

F. Substrate effects on QAH effect

One critical point is whether the QAH effect of the 2D Nb_2O_3 lattice can remain on a substrate, since the substrates are inevitable in device applications [48–51]. The MoS_2 monolayer is chemically inert and does not easily bond strongly with other atoms, thus may be adopted as protective film to growth Nb_2O_3 lattice. Here, we place the Nb_2O_3 lattice on MoS_2 substrate to form a Nb_2O_3/MoS_2 heterostructure, as shown in Fig. 7(a). After structural optimization, the distance of Nb_2O_3 and MoS_2 layers is 3.51 Å with a binding energy of −47 meV per unit cell, suggesting a typical van der Waals structure. In this case, the main features of QAH effect in free-standing Nb_2O_3 lattice remain intact. Figure 7(b) presents the calculated band structure with SOC. As expected, here there is still a SOC-induced gap at the Dirac point around the Fermi level, and the states around the Fermi level are dominantly contributed by the kagome band. Considering the 2D wide gap MoS_2 substrate electrically insulate adjacent QSH layer of the Nb_2O_3 lattice, protecting parallel helical edge channels from being gapped by interlayer hybridization, the Nb_2O_3/MoS_2 heterostructure can parametrically increase the number of edge transport channels to support the dissipationless charge/spin transport in the topological states. These results demonstrate the feasibility of constructing the quantum device by the Nb_2O_3/MoS_2 heterostructure, as illustrated in Fig. 7(c).

IV. CONCLUSION

In summary, we employ DFT calculations to demonstrate the possibility of realizing the intrinsic QAH effect in 2D Nb_2O_3 lattice, and predict that such a lattice is a good candidate. The Curie temperature estimated from the spin-wave model is about $T_C = 392$ K. Also, the nontrivial properties in Dirac bands are confirmed by a nonzero Chern number ($C = 1$), quantized Hall conductivity, and gapless chiral edge states. A TB model is constructed to explain the origin of nontrivial topology. Such a structure is easier to synthesize and much more homogeneous than other QAH insulators, thus enabling the Nb_2O_3 lattice to be a promising platform for realizing low-dissipation topotronics devices.

ACKNOWLEDGMENT

This work was supported by the National Natural Science Foundation of China (Grant No. 11434006).

APPENDIX: DETAILED TIGHT-BINDING MODEL

1. Lattice and Hamiltonian

a. Lattice

Here, we present the proposed lattice model of Nb_2O_3 in Fig. (1). We chose the x and y axes along the armchair and zigzag directions, respectively. The z direction is in the normal direction to the plane of the Nb_2O_3 plane (i.e., xy plane). There are two atoms and two orbitals on each atom in the unit cell. With this definition of coordinates, the lattice vectors are expressed as

$$\begin{aligned}\vec{e}_1 &= \frac{\sqrt{3}}{2}\vec{e}_x + \frac{1}{2}\vec{e}_y,\\ \vec{e}_2 &= -\frac{\sqrt{3}}{2}\vec{e}_x + \frac{1}{2}\vec{e}_y,\\ \vec{e}_3 &= -\vec{e}_y,\\ \vec{\delta}_2 &= \vec{e}_2 - \vec{e}_1,\\ \vec{\delta}_3 &= \vec{e}_3 - \vec{e}_1,\end{aligned} \tag{A1}$$

where $\vec{R}_i = m_i\vec{a} + n_i\vec{b}$ denotes the lattice points of the A site; $\vec{\delta}_j$ is the displacement from a unit cell to its neighboring unit cells, as illustrated in Fig. 1.

b. Method of deriving the Hamiltonian in momentum space from the TB Hamiltonian in real space

We propose a TB Hamiltonian including d_{xz} and d_{yz} atomic orbital. The nearest-neighbor effective TB Hamiltonian without SOC in real space is expressed as

$$H = \sum_{ij,\mu\upsilon} c^{\dagger}_{i\mu} H_{i\mu,j\upsilon} c_{j\upsilon}. \tag{A2}$$

So, the TB Hamiltonian in momentum space can be given by

$$H = \sum_{\vec{k}} \psi^{\dagger}_{\vec{k}} \left(H_{00} + \sum_{\vec{\delta}_j} H_{0\vec{\delta}_j} e^{i\vec{k}\cdot\vec{\delta}_j} \right) \psi_{\vec{k}}, \tag{A3}$$

where the wave functions of Nb atoms can be expressed as

$$\psi = (c_{A\mu}, c_{B\upsilon}, \ldots)^{T}, \tag{A4}$$

$$\psi^{\dagger} = (c^{\dagger}_{A\mu}, c^{\dagger}_{B\upsilon}, \ldots), \tag{A5}$$

where the i and j denote the lattice point of Nb_2O_3 lattice in real space, μ and υ represent the Nb atom in the A1th (first) and Bth (second) sites, respectively.

c. Systematical descriptions on TB Hamiltonian

To accurate to describe the low-energy effective TB Hamiltonian, in the basis of $(d_{A,xz}, d_{A,yz}, d_{B,xz}, d_{B,yz},)^{T}$, we can define the Hamiltonian in real space as $H = H_0 + H_{soc}$. H_0 is the nearest-neighbor hopping term given as

$$H_0 = t \sum_{i,j} \left(d^{\dagger}_{j,\vec{R}_i} d_{j,\vec{R}_i + \vec{e}_j} + \text{H.c.} \right), \tag{A6}$$

where $\vec{R}_i = m_i \vec{a} + n_i \vec{b}$ denotes the lattice points of the A site; $\vec{\delta}_j$ is the displacement from a unit cell to its neighboring unit cells; $\Gamma = xz, yz$ distinguishes different d orbitals on Nb atoms. Also, we define d_j as

$$d_j = (d_{xz}\vec{e}_x + d_{yz}\vec{e}_y) \cdot \vec{e}_j \tag{A7}$$

with the expression of

$$\begin{aligned} d_1 &= \frac{\sqrt{3}}{2} d_{xz} + \frac{1}{2} d_{yz}, \quad d_1^{\dagger} = \frac{\sqrt{3}}{2} d^{\dagger}_{xz} + \frac{1}{2} d^{\dagger}_{yz}, \\ d_2 &= -\frac{\sqrt{3}}{2} d_{xz} + \frac{1}{2} d_{yz}, \quad d_2^{\dagger} = -\frac{\sqrt{3}}{2} d^{\dagger}_{xz} + \frac{1}{2} d^{\dagger}_{yz}, \\ d_3 &= -d_{yz}, \quad d_3^{\dagger} = -d^{\dagger}_{yz}. \end{aligned} \tag{A8}$$

It is known that spin-orbit coupling (SOC) is a relativistic correction of the Schrödinger equation. It can significantly affect the electronic properties of systems that turn it into a topological phase. In such systems, the representation of the SOC Hamiltonian is given as

$$H_{SOC} = i\lambda \sum_i \left[\left(d^{\dagger}_{xz,\vec{R}_i} d_{yz,\vec{R}_i} - d^{\dagger}_{yz,\vec{R}_i} d_{xz,\vec{R}_i} \right) + \left(d^{\dagger}_{xz,\vec{R}_i^{(B)}} d_{yz,\vec{R}_i^{(B)}} - d^{\dagger}_{yz,\vec{R}_i^{(B)}} d_{xz,\vec{R}_i^{(B)}} \right) \right]. \tag{A9}$$

Here, the λ describes the strength of SOC whose value depends on the type of atomic species. Also, we can give the $d^{\dagger}_{1,\vec{0}} d_{1,\vec{e}_1}$, $d^{\dagger}_{2,\vec{0}} d_{2,\vec{e}_2}$, and $d^{\dagger}_{3,\vec{0}} d_{3,\vec{e}_3}$ as follows:

$$\begin{aligned} d^{\dagger}_{1,\vec{0}} d_{1,\vec{e}_1} &= \left(\frac{\sqrt{3}}{2} d^{\dagger}_{xz,} + \frac{1}{2} d^{\dagger}_{yz} \right) \left(\frac{\sqrt{3}}{2} d_{xz,\vec{e}_1} + \frac{1}{2} d_{yz,\vec{e}_1} \right) \\ &= \frac{3}{4} d^{\dagger}_{xz} d_{xz,\vec{e}_1} + \frac{\sqrt{3}}{4} d^{\dagger}_{xz} d_{yz,\vec{e}_1} + \frac{\sqrt{3}}{4} d^{\dagger}_{yz} d_{xz,\vec{e}_1} + \frac{1}{4} d^{\dagger}_{yz} d_{yz,\vec{e}_1}, \\ d^{\dagger}_{2,\vec{0}} d_{2,\vec{e}_2} &= \left(\frac{-\sqrt{3}}{2} d^{\dagger}_{xz,} + \frac{1}{2} d^{\dagger}_{yz} \right) \left(\frac{-\sqrt{3}}{2} d_{xz,\vec{e}_2} + \frac{1}{2} d_{yz,\vec{e}_2} \right) \\ &= \frac{3}{4} d^{\dagger}_{xz} d_{xz,\vec{e}_2} - \frac{\sqrt{3}}{4} d^{\dagger}_{xz} d_{yz,\vec{e}_2} + \frac{\sqrt{3}}{4} d^{\dagger}_{yz} d_{xz,\vec{e}_2} + \frac{1}{4} d^{\dagger}_{yz} d_{yz,\vec{e}_2}, \\ d^{\dagger}_{3,\vec{0}} d_{3,\vec{e}_3} &= d^{\dagger}_{yz} d_{yz,\vec{e}_3}. \end{aligned} \tag{A10}$$

As a consequence, the representation of matrix H_{00} and $H_{0\vec{\delta}_j}$ necessary in Eq. (A9) in the above-mentioned basis is

$$H_{00} = \begin{pmatrix} 0 & i\lambda & \frac{3}{4}t & \frac{\sqrt{3}}{4}t \\ -i\lambda & 0 & \frac{\sqrt{3}}{4}t & \frac{1}{4}t \\ \frac{3}{4}t & \frac{\sqrt{3}}{4}t & 0 & i\lambda \\ \frac{\sqrt{3}}{4}t & \frac{1}{4}t & -i\lambda & 0 \end{pmatrix}, \tag{A11}$$

$$H_{0,\vec{\delta}_2} = \begin{pmatrix} 0 & 0 & \frac{3}{4}t & \frac{-\sqrt{3}}{4}t \\ 0 & 0 & \frac{-\sqrt{3}}{4}t & \frac{1}{4}t \\ 0 & 0 & 0 & 0 \\ 0 & 0 & 0 & 0 \end{pmatrix}, \tag{A12}$$

$$H_{0,\vec{\delta}_3} = \begin{pmatrix} 0 & 0 & 0 & 0 \\ 0 & 0 & 0 & t \\ 0 & 0 & 0 & 0 \\ 0 & 0 & 0 & 0 \end{pmatrix} \tag{A13}$$

with the expression of

$$H_{0,-\vec{\delta}_2} = H^{\dagger}_{0,\vec{\delta}_2}, H_{0,-\vec{\delta}_3} = H^{\dagger}_{0,\vec{\delta}_3}. \tag{A14}$$

According to the definition of TB Hamiltonian, we can obtain the Hamiltonian in momentum space as

$$\begin{aligned} H(\vec{k}) &= H_{00} + \sum_{\vec{\delta}_j} H_{0\delta} e^{i\vec{k}\cdot\vec{\delta}_j} \\ &= \begin{pmatrix} 0 & i\lambda & \frac{3}{4}t & \frac{\sqrt{3}}{4}t \\ -i\lambda & 0 & \frac{\sqrt{3}}{4}t & \frac{1}{4}t \\ \frac{3}{4}t & \frac{\sqrt{3}}{4}t & 0 & i\lambda \\ \frac{\sqrt{3}}{4}t & \frac{1}{4}t & -i\lambda & 0 \end{pmatrix} + \begin{pmatrix} 0 & 0 & \frac{3}{4}te^{i\vec{k}\cdot\vec{\delta}_2} & \frac{-\sqrt{3}}{4}te^{i\vec{k}\cdot\vec{\delta}_2} \\ 0 & 0 & \frac{-\sqrt{3}}{4}te^{i\vec{k}\cdot\vec{\delta}_2} & \frac{1}{4}te^{i\vec{k}\cdot\vec{\delta}_2} \\ \frac{3}{4}te^{-i\vec{k}\cdot\vec{\delta}_2} & \frac{-\sqrt{3}}{4}te^{-i\vec{k}\cdot\vec{\delta}_2} & 0 & 0 \\ \frac{-\sqrt{3}}{4}te^{-i\vec{k}\cdot\vec{\delta}_2} & \frac{1}{4}te^{-i\vec{k}\cdot\vec{\delta}_2} & 0 & 0 \end{pmatrix} \\ &+ \begin{pmatrix} 0 & 0 & te^{i\vec{k}\cdot\vec{\delta}_3} & \\ 0 & 0 & & 0 \\ te^{-i\vec{k}\cdot\vec{\delta}_3} & & 0 & 0 \\ & 0 & 0 & \end{pmatrix} = \begin{pmatrix} 0 & i\lambda & tg_1 & tg_2 \\ -i\lambda & 0 & tg_2 & tg_3 \\ tg_1^* & tg_2^* & 0 & i\lambda \\ tg_2^* & tg_3^* & -i\lambda & 0 \end{pmatrix}. \end{aligned} \tag{A15}$$

Here the corresponding terms of g_1, g_2, and g_3 are expressed as

$$\begin{aligned} g_1 &= \frac{3}{4} + \frac{3}{4}e^{i\vec{k}\cdot\vec{\delta}_2}, \\ g_2 &= \frac{\sqrt{3}}{4} - \frac{\sqrt{3}}{4}e^{i\vec{k}\cdot\vec{\delta}_2}, \\ g_3 &= \frac{1}{4} + \frac{1}{4}e^{i\vec{k}\cdot\vec{\delta}_2} + e^{i\vec{k}\cdot\vec{\delta}_3}. \end{aligned} \tag{A16}$$

Finally, in the basis $(e^{i\vec{k}\cdot\vec{e}_1}d_{A,xz}, e^{i\vec{k}\cdot\vec{e}_1}d_{A,yz}, d_{B,xz}, d_{B,yz},)^T$, the TB Hamiltonian of the Nb_2O_3 lattice becomes

$$\begin{aligned} PHP^{\dagger} &= \begin{pmatrix} e^{i\vec{k}\cdot\vec{e}_1} & 0 & 0 & 0 \\ 0 & e^{i\vec{k}\cdot\vec{e}_1} & 0 & 0 \\ 0 & 0 & 1 & 0 \\ 0 & 0 & 0 & 1 \end{pmatrix} \begin{pmatrix} 0 & i\lambda & tg_1 & tg_2 \\ -i\lambda & 0 & tg_2 & tg_3 \\ tg_1^* & tg_2^* & 0 & i\lambda \\ tg_2^* & tg_3^* & -i\lambda & 0 \end{pmatrix} \begin{pmatrix} e^{-i\vec{k}\cdot\vec{e}_1} & 0 & 0 & 0 \\ 0 & e^{-i\vec{k}\cdot\vec{e}_1} & 0 & 0 \\ 0 & 0 & 1 & 0 \\ 0 & 0 & 0 & 1 \end{pmatrix} \\ &= \begin{pmatrix} 0 & i\lambda & tg_1e^{i\vec{k}\cdot\vec{e}_1} & tg_2e^{i\vec{k}\cdot\vec{e}_1} \\ -i\lambda & 0 & tg_1e^{i\vec{k}\cdot\vec{e}_1} & tg_3e^{i\vec{k}\cdot\vec{e}_1} \\ tg_1^*e^{-i\vec{k}\cdot\vec{e}_1} & tg_2^*e^{-i\vec{k}\cdot\vec{e}_1} & 0 & i\lambda \\ tg_2^*e^{-i\vec{k}\cdot\vec{e}_1} & tg_3^*e^{-i\vec{k}\cdot\vec{e}_1} & -i\lambda & 0 \end{pmatrix} = \begin{pmatrix} 0 & i\lambda & tg_1' & tg_2' \\ -i\lambda & 0 & tg_2' & tg_3' \\ tg_1'^* & tg_2'^* & 0 & i\lambda \\ tg_2'^* & tg_3'^* & -i\lambda & 0 \end{pmatrix}, \end{aligned} \tag{A17}$$

where the corresponding parameters of g_1',g_2', and g_3' are given by

$$\begin{aligned} g_1' &= g_1e^{i\vec{k}\cdot\vec{e}_1} = \frac{3}{4}e^{i\vec{k}\cdot\vec{e}_1} + \frac{3}{4}e^{i\vec{k}\cdot\vec{e}_2}, \\ g_2' &= g_2e^{i\vec{k}\cdot\vec{e}_1} = \frac{\sqrt{3}}{4}e^{i\vec{k}\cdot\vec{e}_1} - \frac{\sqrt{3}}{4}e^{i\vec{k}\cdot\vec{e}_2}, \\ g_3' &= g_3e^{i\vec{k}\cdot\vec{e}_1} = \frac{1}{4}e^{i\vec{k}\cdot\vec{e}_1} + \frac{1}{4}e^{i\vec{k}\cdot\vec{e}_2} + e^{i\vec{k}\cdot\vec{e}_3}. \end{aligned} \tag{A18}$$

In the basis of $(d_{A,+}, d_{A,-}, d_{B,+}, d_{B,-})^T$, we further can obtain

$$\begin{pmatrix} d_{A,+} \\ d_{A,-} \\ d_{B,+} \\ d_{B,-} \end{pmatrix} = P \begin{pmatrix} e^{i\vec{k}\cdot\vec{e}_1}d_{A,xz} \\ e^{i\vec{k}\cdot\vec{e}_1}d_{A,yz} \\ d_{B,xz} \\ d_{B,yz} \end{pmatrix}, \quad P = \frac{1}{\sqrt{2}} \begin{pmatrix} 1 & -i & 0 & 0 \\ 1 & i & 0 & 0 \\ 0 & 0 & 1 & -i \\ 0 & 0 & 1 & i \end{pmatrix},$$

$$PHP^{\dagger} = \frac{1}{2} \begin{pmatrix} 1 & -i & 0 & 0 \\ 1 & i & 0 & 0 \\ 0 & 0 & 1 & -i \\ 0 & 0 & 1 & i \end{pmatrix} \begin{pmatrix} 0 & i\lambda & tg_1' & tg_2' \\ -i\lambda & 0 & tg_2' & tg_3' \\ tg_1'^* & tg_2'^* & 0 & i\lambda \\ tg_2'^* & tg_3'^* & -i\lambda & 0 \end{pmatrix} \begin{pmatrix} 1 & 1 & 0 & 0 \\ i & -i & 0 & 0 \\ 0 & 0 & 1 & 1 \\ 0 & 0 & i & -i \end{pmatrix}$$

$$= \frac{1}{2}\begin{pmatrix} -\lambda & i\lambda & t(g_1' - ig_2') & t(g_2' - ig_3') \\ \lambda & i\lambda & t(g_1' + ig_2') & t(g_2' + ig_3') \\ t(g_1'^* - ig_2'^*) & t(g_2'^* - ig_3'^*) & -\lambda & i\lambda \\ t(g_1'^* + ig_2'^*) & t(g_2'^* + ig_3'^*) & \lambda & i\lambda \end{pmatrix}\begin{pmatrix} 1 & 1 & 0 & 0 \\ i & -i & 0 & 0 \\ 0 & 0 & 1 & 1 \\ 0 & 0 & i & -i \end{pmatrix}$$

$$= \begin{pmatrix} -\lambda & 0 & \frac{1}{2}t(g_1' + g_3') & \frac{1}{2}t(g_2' - g_3' - i2g_2') \\ 0 & \lambda & \frac{1}{2}t(g_1' - g_3' + i2g_2') & \frac{1}{2}t(g_1' + g_3') \\ \frac{1}{2}t(g_1'^* + g_3'^*) & \frac{1}{2}t(g_1'^* - i2g_2'^* - g_3'^*) & -\lambda & 0 \\ \frac{1}{2}t(g_1'^* + ig_2'^* - g_3'^*) & \frac{1}{2}t(g_2'^* + g_3'^*) & 0 & \lambda \end{pmatrix}. \tag{A19}$$

Here, the corresponding parameters should correspond to

$$g_1' = g_1 e^{i\vec{k}\cdot\vec{e}_1} = \frac{3}{4}e^{i\vec{k}\cdot\vec{e}_1} + \frac{3}{4}e^{i\vec{k}\cdot\vec{e}_2},$$

$$g_2' = g_2 e^{i\vec{k}\cdot\vec{e}_1} = \frac{\sqrt{3}}{4}e^{i\vec{k}\cdot\vec{e}_1} - \frac{\sqrt{3}}{4}e^{i\vec{k}\cdot\vec{e}_2}, \tag{A20}$$

$$g_3' = g_3 e^{i\vec{k}\cdot\vec{e}_1} = \frac{1}{4}e^{i\vec{k}\cdot\vec{e}_1} + \frac{1}{4}e^{i\vec{k}\cdot\vec{e}_2} + e^{i\vec{k}\cdot\vec{e}_3},$$

$$g_1' + g_3' = e^{i\vec{k}\cdot\vec{e}_1} + e^{i\vec{k}\cdot\vec{e}_2} + e^{i\vec{k}\cdot\vec{e}_3}, \tag{A21}$$

$$\begin{aligned} g_1' - g_3' - i2g_2' &= \frac{1}{2}e^{i\vec{k}\cdot\vec{e}_1} - i\frac{\sqrt{3}}{2}e^{i\vec{k}\cdot\vec{e}_1} + \frac{1}{2}e^{i\vec{k}\cdot\vec{e}_2} + i\frac{\sqrt{3}}{2}e^{i\vec{k}\cdot\vec{e}_2} - e^{i\vec{k}\cdot\vec{e}_3} \\ &= \frac{1 - i\sqrt{3}}{2}e^{i\vec{k}\cdot\vec{e}_1} + \frac{1 + i\sqrt{3}}{2}e^{i\vec{k}\cdot\vec{e}_2} - e^{i\vec{k}\cdot\vec{e}_3} \\ &= e^{-i(\pi/3)}e^{i\vec{k}\cdot\vec{e}_1} + e^{-i(5\pi/3)}e^{i\vec{k}\cdot\vec{e}_2} + e^{-i3\pi}e^{i\vec{k}\cdot\vec{e}_3}, \end{aligned} \tag{A22}$$

$$\begin{aligned} g_1' - g_3' + i2g_2' &= \frac{1}{2}e^{i\vec{k}\cdot\vec{e}_1} + i\frac{\sqrt{3}}{2}e^{i\vec{k}\cdot\vec{e}_1} + \frac{1}{2}e^{i\vec{k}\cdot\vec{e}_2} - i\frac{\sqrt{3}}{2}e^{i\vec{k}\cdot\vec{e}_2} - e^{i\vec{k}\cdot\vec{e}_3} \\ &= \frac{1 + i\sqrt{3}}{2}e^{i\vec{k}\cdot\vec{e}_1} + \frac{1 - i\sqrt{3}}{2}e^{i\vec{k}\cdot\vec{e}_2} - e^{i\vec{k}\cdot\vec{e}_3} \\ &= e^{i(\pi/3)}e^{i\vec{k}\cdot\vec{e}_1} + e^{i(5\pi/3)}e^{i\vec{k}\cdot\vec{e}_2} + e^{i3\pi}e^{i\vec{k}\cdot\vec{e}_3}. \end{aligned} \tag{A23}$$

By defining $e^{i\vec{k}\cdot\vec{e}_j} = b_j$, $\theta_j = 1,2,3 = (\frac{\pi}{6}, \frac{5\pi}{6}, \frac{3\pi}{2})$, then we have the Hamiltonian

$$H(\vec{k}) = \begin{pmatrix} -\lambda & 0 & \frac{1}{2}t\sum_j b_j & \frac{1}{2}t\sum_j e^{-2i\theta_j}b_j \\ 0 & \lambda & \frac{1}{2}t\sum_j e^{2i\theta_j}b_j & \frac{1}{2}t\sum_j b_j \\ \frac{1}{2}t\sum_j b_j^* & \frac{1}{2}t\sum_j e^{-2i\theta_j}b_j^* & -\lambda & 0 \\ \frac{1}{2}t\sum_j e^{2i\theta_j}b_j^* & \frac{1}{2}t\sum_j b_j^* & 0 & \lambda \end{pmatrix}. \tag{A24}$$

Obviously, the derived Hamiltonian is identical to the one given in Eq. (3) in our original paper.

2. Model to estimate the TB parameters

From Eq. (A24), we can infer the TB Hamiltonian as

$$H(\vec{k}) = \begin{pmatrix} -\lambda & 0 & \frac{t}{2}g(\vec{k}) & \frac{t}{2}l(\vec{k}) \\ 0 & \lambda & \frac{t}{2}m(\vec{k}) & \frac{t}{2}g(\vec{k}) \\ \frac{t}{2}g^*(\vec{k}) & \frac{t}{2}m^*(\vec{k}) & -\lambda & 0 \\ \frac{t}{2}l^*(\vec{k}) & \frac{t}{2}g^*(\vec{k}) & 0 & \lambda \end{pmatrix}, \tag{A25}$$

where

$$
\begin{aligned}
g(\vec{k}) &= e^{i\vec{k}\cdot\vec{e}_1} + e^{i\vec{k}\cdot\vec{e}_2} + e^{i\vec{k}\cdot\vec{e}_3},\\
l(\vec{k}) &= \frac{1-i\sqrt{3}}{2}e^{i\vec{k}\cdot\vec{e}_1} + \frac{1+i\sqrt{3}}{2}e^{i\vec{k}\cdot\vec{e}_2} - e^{i\vec{k}\cdot\vec{e}_3},\\
m(\vec{k}) &= \frac{1+i\sqrt{3}}{2}e^{i\vec{k}\cdot\vec{e}_1} + \frac{1-i\sqrt{3}}{2}e^{i\vec{k}\cdot\vec{e}_2} - e^{i\vec{k}\cdot\vec{e}_3},
\end{aligned}
\tag{A26}
$$

and

$$
\begin{aligned}
\vec{k}\cdot\vec{e}_1 &= \frac{\sqrt{3}}{2}k_x + \frac{1}{2}k_y,\\
\overrightarrow{k}\cdot\vec{e}_2 &= \frac{-\sqrt{3}}{2}k_x + \frac{1}{2}k_y,\\
\vec{k}\cdot\vec{e}_3 &= -k_y.
\end{aligned}
\tag{A27}
$$

3. On-site energy term in TB Hamiltonian

In the basis of $(d_{A,xz},d_{A,yz},d_{B,xz},d_{B,yz,})^T$, the on-site term should be expressed as $H_{ii} = \mathrm{diag}(\epsilon_{Axz},\epsilon_{Ayz},\epsilon_{Bxz},\epsilon_{Byz})$. However, in the basis of $(d_{A,+},d_{A,-},d_{B,+},d_{B,-,})^T$, this expression becomes

$$
\begin{aligned}
PH_{ii}P^\dagger &= \frac{1}{2}\begin{pmatrix} 1 & -i & 0 & 0\\ 1 & -i & 0 & 0\\ 0 & 0 & 1 & -i\\ 0 & 0 & 1 & -i \end{pmatrix}
\begin{pmatrix} \epsilon_{Axz} & 0 & 0 & 0 & 0\\ 0 & 0 & 0 & 0 & 0\\ 0 & 0 & \epsilon_{Ayz} & 0 & 0\\ 0 & 0 & 0 & \epsilon_{B,xz} & 0\\ 0 & 0 & 0 & 0 & \epsilon_{B,yz} \end{pmatrix}
\begin{pmatrix} 1 & 1 & 0 & 0\\ i & -i & 0 & 0\\ 0 & 0 & 1 & 1\\ 0 & 0 & i & -i \end{pmatrix}\\
&= \frac{1}{2}\begin{pmatrix} \epsilon_{Axz}+\epsilon_{Ayz} & \epsilon_{Axz}-\epsilon_{Ayz} & 0 & 0\\ \epsilon_{Axz}-\epsilon_{Ayz} & \epsilon_{Axz}+\epsilon_{Ayz} & 0 & 0\\ 0 & 0 & \epsilon_{Bxz}+\epsilon_{Byz} & \epsilon_{Bxz}-\epsilon_{Byz}\\ 0 & 0 & \epsilon_{Bxz}-\epsilon_{Byz} & \epsilon_{Bxz}+\epsilon_{Byz} \end{pmatrix}.
\end{aligned}
\tag{A28}
$$

In this case, when the on-site component is added, the TB Hamiltonian becomes

$$
H(\vec{k}) = \begin{pmatrix} -\lambda + \frac{\epsilon_{Axz}+\epsilon_{Ayz}}{2} & \frac{\epsilon_{Axz}-\epsilon_{Ayz}}{2} & \frac{t}{2}g(\vec{k}) & \frac{t}{2}l(\vec{k})\\ \frac{\epsilon_{Axz}-\epsilon_{Ayz}}{2} & \lambda + \frac{\epsilon_{Axz}+\epsilon_{Ayz}}{2} & \frac{t}{2}m(\vec{k}) & \frac{t}{2}g(\vec{k})\\ \frac{t}{2}g^*(\vec{k}) & \frac{t}{2}m^*(\vec{k}) & -\lambda + \frac{\epsilon_{Bxz}+\epsilon_{Byz}}{2} & \frac{\epsilon_{Bxz}-\epsilon_{Byz}}{2}\\ \frac{t}{2}l^*(\vec{k}) & \frac{t}{2}g^*(\vec{k}) & \frac{\epsilon_{Bxz}-\epsilon_{Byz}}{2} & \lambda + \frac{\epsilon_{Bxz}+\epsilon_{Byz}}{2} \end{pmatrix}.
\tag{A29}
$$

Obviously, this expression may be simplified if all four orbits share the same energy, which means $\epsilon_{Axz} = \epsilon_{Ayz} = \epsilon_{Bxz} = \epsilon_{Byz}$.

[1] H. J. Zhang, J. Wang, G. Xu, Y. Xu, and S. C. Zhang, Phys. Rev. Lett. **112**, 096804 (2014).

[2] J. G. Checkelsky, R. Yoshimi, A. Tsukazaki, K. S. Takahashi, Y. Kozuka, J. Falson, M. Kawasaki, and Y. Tokura, Nat. Phys. **10**, 731 (2014).

[3] J. Wu, J. Liu, and X. J. Liu, Phys. Rev. Lett. **113**, 136403 (2014).

[4] N. Nagaosa, J. Sinova, S. Onoda, A. H. MacDonald, and N. P. Ong, Rev. Mod. Phys. **82**, 1539 (2010).

[5] Z. Qiao, W. Ren, H. Chen, L. Bellaiche, Z. Zhang, A. H. MacDonald, and Q. Niu, Phys. Rev. Lett. **112**, 116404 (2014).

[6] R. W. Zhang, C. W. Zhang, W. X. Ji, P. Li, P. J. Wang, S. S. Li, and S. S. Yan, Appl. Phys. Lett. **109**, 182109 (2016).

[7] W. Luo and H. J. Xiang, Nano Lett. **15**, 3230 (2015).

[8] L. Fu, C. L. Kane, and E. J. Mele, Phys. Rev. Lett. **98**, 106803 (2007).

[9] Y. P. Wang, W. X. Ji, C. W. Zhang, P. Li, F. Li, P. J. Wang, S. S. Li, and S. S. Yan, Appl. Phys. Lett. **108**, 073104 (2016).

[10] C. Z. Chang, J. Zhang, X. Feng, J. Shen, Z. Zhang, M. Guo, K. Li, Y. Ou, P. Wei, L. L. Wang, Z. Q. Ji, Y. Feng, S. Ji, X. Chen, J. Jia, X. Dai, Z. Fang, S. C. Zhang, K. He, Y. Wang *et al.*, Science **340**, 167 (2013).

[11] X. Kou, S.T. Guo, Y. Fan, L. Pan, M. Lang, Y. Jiang, Q. Shao, T. Nie, K. Murata, J. Tang, Y. Wang, L. He, T. K. Lee, W. L. Lee, and K. L. Wang, Phys. Rev. Lett. **113**, 137201 (2014).

[12] K. Dolui, S. Ray, and T. Das, Phys. Rev. B **92**, 205133 (2015).

[13] J. Zhang, B. Zhao, Y. Yao, and Z. Yang, Phys. Rev. B **92**, 165418 (2015).

[14] C. X. Liu, S.C. Zhang, and X. L. Qi, Annu. Rev. Condens. Matter Phys. **7**, 301 (2016).

[15] F. D. M. Haldane, Phys. Rev. Lett. **61**, 2015 (1988).

[16] X. Zhang and S.-C. Zhang, Proc. SPIE **8373**, 837309 (2012).
[17] D. Xiao, W. Zhu, Y. Ran, N. Nagaosa, and S. Okamoto, Nat. Commun. **2**, 596 (2011).
[18] H. Zhang, C. Lazo, S. Blügel, S. Heinze, and Y. Mokrousov, Phys. Rev. Lett. **108**, 056802 (2012).
[19] Z. Wang, C. Tang, R. Sachs, Y. Barlas, and J. Shi, Phys. Rev. Lett. **114**, 016603 (2015).
[20] X. L. Zhang, L. F. Liu, and W. M. Liu, Sci. Rep. **3**, 2908 (2013).
[21] S. C. Wu, G. Shan, and B. Yan, Phys. Rev. Lett. **113**, 256401 (2014).
[22] G. Xu, B. Lian, and S. C. Zhang, Phys. Rev. Lett. **115**, 186802 (2015).
[23] Y. P. Wang, W. X. Ji, C. W. Zhang, P. Li, P. J. Wang, B. Kong, S. S. Li, S. S. Yan, and K. Liang, Appl. Phys. Lett. **110**, 233107 (2017).
[24] G. Kresse and J. Furthmüller, Phys. Rev. B **54**, 11169 (1996).
[25] P. E. Blöchl, Phys. Rev. B **50**, 17953 (1994).
[26] G. Kresse and D. Joubert, Phys. Rev. B **59**, 1758 (1999).
[27] J. P. Perdew, K. Burke, and M. Ernzerhof, Phys. Rev. Lett. **77**, 3865 (1996).
[28] G. De Fusco, B. Montanari, and N. M. Harrison, Phys. Rev. B **82**, 220404 (2010).
[29] J. Paier, M. Marsman, K. Hummer, G. Kresse, I. C. Gerber, and J. G. Ángyán. J. Chem. Phys. **124**, 154709 (2006).
[30] A. Togo, F. Oba, and I. Tanaka, Phys. Rev. B **78**, 134106 (2008).
[31] Z. F. Wang, Z. Liu, and F. Liu, Nat. Commun. **4**, 1471 (2013).
[32] Z. Liu, Z. F. Wang, J. W. Mei, Y. S. Wu, and F. Liu, Phys. Rev. Lett. **110**, 106804 (2013).
[33] X. Zhang, Z. Wang, M. Zhao, and F. Liu, Phys. Rev. B **93**, 165401 (2016).
[34] See Supplemental Material at http://link.aps.org/supplemental/10.1103/PhysRevB.96.205433 for the structure of Nb_2O_3: the MD simulations at different temperatures, band structures with respect to different U value, and investigation of energy differences as a function of U value for Nb_2O_3 lattice.
[35] R. Addou, A. Dahal, and M. Batzill, Nat. Nanotechnol. **8**, 41 (2013).
[36] T. T. Song, M. Yang, J. W.Chai, M. Callsen, J. Zhou, T. Yang, Z. Zhang, J. S. Pan, D. Z. Chi, Y. P. Feng, and S. J. Wang, Sci. Rep. **6**, 29221 (2016).
[37] N. D. Mermin and H. Wagner, Phys. Rev. Lett. **17**, 1133 (1966).
[38] J. L. Lado and J. Fernández-Rossier, 2D Mater. **4**, 035002 (2017).
[39] C. L. Kane and E. J. Mele, Phys. Rev. Lett. **95**, 226801 (2005).
[40] C. C. Liu, W. X. Feng, and Y. G. Yao, Phys. Rev. Lett. **107**, 076802 (2011).
[41] M. P. L. Sancho, J. M. L. Sancho, J. M. L. Sancho, and J. Rubio, J. Phys. F **15**, 851 (1985).
[42] N. Marzari and D. Vanderbilt, Phys. Rev. B **56**, 12847 (1997).
[43] I. Souza, N. Marzari, and D. Vanderbilt, Phys. Rev. B **65**, 035109 (2001).
[44] Y. G. Yao, L. Kleinman, A. H. MacDonald, J. Sinova, T. Jungwirth, D. S. Wang, E. Wang, and Q. Niu, Phys. Rev. Lett. **92**, 037204 (2004).
[45] Y. G. Yao and Z. Fang, Phys. Rev. Lett. **95**, 156601 (2005).
[46] Y. Guo, Y. F. Zhang, X. Y. Bao, T. Z. Han, Z. Tang, L. X. Zhang, W. G. Zhu, E. G. Wang, Q. Niu, Z. Q. Qiu, J. F. Jia, Z. X. Zhao, and Q. K. Xue, Science **306**, 1915 (2004).
[47] L. Ju, J. Velasco Jr, E. Huang, S. Kahn, C. Nosiglia, H. Z. Tsai, W. Yang, T. Taniguchi, K. Watanabe, Y. Zhang, G. Zhang, M. Crommie, A. Zettl, and F. Wang, Nat. Nanotechnol. **9**, 348 (2014).
[48] R. W. Zhang, C. W. Zhang, W. X. Ji, S. S. Li, S. J. Hu, S. S. Yan, P. Li, P. J. Wang, and F. Li, New J. Phys. **17**, 083036 (2015).
[49] H. Zhao, C. W. Zhang, W. X. Ji, R. W. Zhang, S. S. Li, S. S. Yan, B. M. Zhang, and P. J. Wang, Sci. Rep. **6**, 20152 (2016).
[50] R. W. Zhang, W. X. Ji, C. W. Zhang, S. S. Li, P. Li, and P. J. Wang, J Mater. Chem. C **4**, 2088 (2016).
[51] M. Zhou, Z. Liu, W. M. Ming, Z. F. Wang, and F. Liu, Phys. Rev. Lett. **113**, 236802 (2014).